Solid State Sciences 143 (2023) 107282

Contents lists available at ScienceDirect

Solid State Sciences

journal homepage: www.elsevier.com/locate/ssscie

Facile synthesis and characterization of ZnO:Al/ZnS/NiO heterojunction thin films with enhanced photocatalytic activities

S. Besra [a], K. Belakroum [a,**], S. Iaiche [b], D. Aouf [c], Y. Rahmani [d], H. Belkhalfa [d], A. Henni [c,*]

[a] Laboratory of New and Renewable Energies Development in Arid and Saharan Zones, University Kasdi Merbah, 30000, Ouargla, Algeria
[b] Laboratory of Structures, Proprieties and Inter Atomic Interactions (LASPI2A), University of Abbes Laghrour, Khenchela, 40000, Algeria
[c] Laboratory of Dynamic Interactions and Reactivity of Systems, University of Kasdi Merbah, 30000, Ouargla, Algeria
[d] Scientific and Technical Research Center in Physicochemical Analysis, Bou-Ismail, Tipaza, Algeria

ARTICLE INFO

Keywords:
ZnO:Al/ZnS/NiO
Multilayer thin films
Spin coating
Spray pyrolysis
Photocatalysis
Visible irradiation

ABSTRACT

This study covers a physical investigation of ZnO:Al/ZnS/NiO heterojunction thin films and their photocatalytic activities. The obtained samples were analyzed using XRD, FTIR, SEM/EDS, AFM, and UV–vis spectroscopy. The XRD and FTIR results confirmed that the nanocrystalline ZnO, ZnS, and NiO phases were successfully prepared. SEM morphological analysis of the multilayer film indicated that depositing different nanocrystalline layers above one another could deteriorate the adherence of the upper layer. In addition, AFM shows acceptable surface roughness for application as a photocatalyst. Optical analysis revealed that the ZnO:Al/ZnS/NiO multilayer film exhibited an average transmittance of 65%. The Eg value of the ZnO:Al monolayer of 3.26 eV is decreased to 3.15 eV after Al–ZnO/ZnS coupling, whereas ZnO:Al/ZnS/NiO exhibits an additional absorption value of 3.52 eV due to the NiO layer. The photocatalytic activity of ZnO:Al/ZnS/NiO under visible light exhibited an approximately 96% photodegradation efficiency against methylene blue after only 50 min. However, under sunlight, the degradation rates reached 90, 85, and 65% for methylene blue, crystal violet, and Congo red, respectively, in 90 min. This study shows that a synthesized ZnO:Al/ZnS/NiO heterojunction multilayer photocatalyst can efficiently degrade organic pollutants.

1. Introduction

The rapid growth of global environmental pollution generated by hazardous waste is caused by rapid industrial development worldwide [1]. In addition, the continuous discharge of pollutants in water resources, such as organic dyes, is the most common type of pollutant because of their solubility and stability in natural water systems and their impact on human and aquatic life [1–3]. These environmental concerns and ever-increasing energy demands have hurried the efforts of active research to develop eco-friendly, modern, harmless, and low-cost techniques to solve these problems [2,4]. Consequently, many researchers have extensively investigated the exclusive properties of nanostructured thin films that belong to the semiconductor family, as demonstrated by experimental and theoretical studies. They are employed in a variety of prospective applications [5,6], such as gas sensors [6], antimicrobial [7], antibacterial [8], and photocatalytic degradation of organic dyes [9]. Photocatalytic is a promising, inexpensive, and beneficial process to eliminate the problem of contaminated wastewater because they exhibit considerable degradation efficiency without involving complex technologies [2,3,10]. In this regard, a considerable number of investigated semiconductor metal oxides-based materials, particularly ZnO and NiO have attracted attention because of their diverse proprieties. Zinc oxide (ZnO) is a promising n-type binary semiconductor of the II-VI group with a wide optical gap energy of 3.37 eV. This makes ZnO suitable for photonic applications in the ultraviolet region [11]. ZnO has two phases, a wurtzite hexagonal structure and a cubic one in its bulk form [5]. Nickel oxide is a p-type semiconductor of the VIII–VI group with a NaCl structure [12], an antiferromagnetic oxide semiconductor [13], transparent with a broad optical gap energy from 3.6 to 4.0 eV [12]. Similarly, thin-film semiconductors based on metal sulfides, such as ZnS, PbS, CuS, and CdS, etc [14,15] have received considerable attention owing to their remarkable properties [14]. ZnS is an n-type semiconductor of the II-VI group with Eg ranging from 3.54 to 3.72 eV for the cubic phase and from 3.74 to

* Corresponding author.
** Corresponding author.
E-mail addresses: karima.belakroum@gmail.com (K. Belakroum), henni.abdellah@gmail.com, henni.abdellah@univ-ouargla.dz (A. Henni).

https://doi.org/10.1016/j.solidstatesciences.2023.107282
Received 4 June 2023; Received in revised form 25 July 2023; Accepted 7 August 2023
Available online 9 August 2023

3.91 eV for the hexagonal one [16]. ZnS is mostly used as a window film for photovoltaic means, such as light-emitting diodes and catalysts [17,18], owing to its good transmittance in the UV–visible range and a large index of refraction [16,19].

Various methods have been employed to prepare thin films, including electrodeposition [20], pulsed laser ablation [21], sputtering [22], sol-gel [14], and spray pyrolysis [23,24]. Among the common methods, sol-gel (dip/spin) and spray pyrolysis are simple and low-cost deposition processes for various metal sulfide/oxide thin films on different substrates such as Si, ITO, FTO, and glass substrates. Among the available alternative semiconductor-deposited thin films, multilayer structures consisting of two or more layers of semiconductor structures have focused on optoelectronic applications [10,25] owing to their good electrical and optical characteristics compared to common monolayers [14], while few studies exist on photocatalytic applications [10]. Furthermore, compared with powder nanoparticles, thin films offer several advantages in the photocatalytic process: they are easy to use/reuse and control and avoid costly powder cleaning/recycling after every degradation [14].

The use of semiconductors as photocatalysts has improved their large performance under various light sources [26], but their excitement by irradiation quickly creates electron-hole pairs, which can take part in a chemical reaction [10], weakening the process [27], and significantly challenging aspects of the photocatalytic performance [2]. To enhance this performance, first, the rate of e-h pair recombination should be reduced, which can occur by different methods, such as adding surface defects [28] and doping with cationic dopants like Li, Al, Co, Fe [6,29–31], rare-earth [32], and heterogeneous (p-n) semiconductors (multilayer) [33–35]. Indeed, choosing semiconductor thin films as photocatalysts not only affects their intrinsic properties, but also their synthesis conditions, which influence the obtained physical properties of the samples. Generally, the photocatalytic activity of ZnO thin films can be enhanced or improved by doping them. Because Al^{3+} has a shorter ionic radius than Zn^{2+} [10], it is a promising dopant for ZnO (AZO), which was previously investigated in the literature [29,36]. Moreover, the AZO sample can couple with other metal oxide phases such as ZnO/AZO/ZnO [10], or metal sulfides like Al–ZnO/ZnS heterostructures [37], which have shown good photocatalytic performance for MB.

This study aimed to synthesize ZnO:Al/ZnS/NiO heterojunction multilayers as photocatalysts for the decomposition of organic dyes using low-cost spin-coating and spray pyrolysis techniques. The properties of the samples were investigated using structural, morphological, and optical characterization tools. To our knowledge, for the first time ZnO:Al/ZnS/NiO has been fabricated as a multilayer thin-film material for dye removal.

2. Experimental details

2.1. Preparation of signal/multilayer thin films

This study uses nanocrystalline films ZnO:Al single-layer, ZnO:Al/ZnS bi-layer, and ZnO:Al/ZnS/NiO tri-layer (labeled as AZ, AZS, and AZSN, respectively) were prepared on glass substrates. First, the glass substrates were cleaned with ethanol in an ultrasonic bath and then with deionized water for 15 min to eliminate any pollutants on their surfaces.

We fabricated an Al-doped ZnO (AZ) thin layer as the first and bottom film by spin coating using an aqueous solution of 0.1 M zinc acetate dihydrate (Zn $(CH_3COO)_2{\cdot}2H_2O$) and 2 wt% of aluminum acetate (Al $(OH)_2$ (CH_3COO)) as the aluminum source. The ZnO:Al solution was prepared by dissolving zinc acetate in the solvent using absolute ethanol (C_2H_6O) in the presence of monoethanolamine (MEA: C_2H_7NO) as the stabilizer. The precursor and stabilizer (MEA) molar ratios were maintained at 1:2. The solution was stirred for 2 h at 75 °C using a magnetic stirrer to obtain a transparent homogeneous sol, which was then stored for 48 h before use. The obtained sol was then deposited on the substrate using a spin-coating method (1500 rpm, 25 s) at ambient temperature. Each coating film was dried at 200 °C for 10 min to evaporate the solvents, and the spin-drying procedure was repeated six times to obtain a film with an acceptable thickness. Finally, the samples were annealed at 500 °C for 90 min.

To obtain AZS and AZSN multilayer thin films, ZnS and ZnS/NiO layers were deposited via spray pyrolysis. Typically, solutions were prepared independently using an appropriate amount of zinc acetate dihydrate (Zn $(CH_3COO)_2{\cdot}2H_2O$) with thiourea (SC $(NH_2)_2$) and nickel chloride hexahydrate ($NiCl_2{\cdot}6H_2O$) as the starting precursors. First, 0.1 M $Zn(CH_3COO)_2{\cdot}2H_2O$ and 0.1 M $SC(NH_2)_2$ were dissolved at 80 °C in deionized water (molar ratio of Zn^{2+} to S^{2-} was 1:1), and then drops of acetic acid were added to inhibit solution deposition. A NiO solution was obtained by dissolving 0.1 M nickel chloride in deionized water at 80 °C. To obtain the AZS and AZSN samples, the prepared precursor solutions were sprayed onto a preheated ZnO:Al-coated substrate at 450 °C. The flow spray rate was 5 ml/min at a distance (nozzle−substrate) of ~35 cm, with a nozzle diameter of 0.3 mm, and deposition time of 8–10 min.

2.2. Characterizations tools of signal/multilayer thin films

After the deposition of the thin layers, it was necessary to characterize them and discuss their physical properties. The crystalline phase structure was determined using Copper radiation $\lambda_{K\alpha} = 1.54$ Å of XR diffractometer using a PANalytical Empyrean diffractometer. The XRD data were recorded in the 2θ range of 10°–70° with a step width of 0.02. Optical analysis was performed using a UV–Vis spectrophotometer (Cary 100 UV–Vis at 200–900 nm). A Cary 660 FTIR spectrometer was used to record attenuated total reflectance (ATR-FTIR) spectra. The surface morphology was investigated using atomic force microscopy (AFM, APE Research A100 AFM) and scanning electron microscopy (SEM, ZEISS EVO 15) equipped with energy dispersive X-ray spectroscopy (EDS). Subsequently, the obtained samples underwent photodegradation of the organic dyes.

2.3. The photocatalytic test (photodegradation measurement)

The photocatalytic activity was investigated by the degradation of a 25 ml aqueous solution of 5 mg/L methylene blue (MB; $C_{16}H_{18}C_lN_3S$) dye, which acts as a representative dye pollutant, with a pH of ~6 in the presence of elaborated films (15 cm^2). The Photodegradation of MB was done by two different irradiation sources, exposed to visible light for 75 min with a 1000 W Halogen lamp, and sunlight by using natural light in May 2022 in Ouargla- Algeria. In addition, crystal violet (CV) and Congo red (CR) dyes were used as pollutants under the same MB degradation conditions but only under sunlight irradiation. Before irradiation, the dye adsorption was performed in the dark for half an hour to achieve equilibrium. The photocatalytic degradation process was monitored by measuring the absorbance of dye (λ_{max}). The process efficiency was evaluated using Eq. (1) [6]:

$$\text{Dye degradation rate } \% = \left(\frac{C_I - C_t}{C_I}\right) \times 100 = \left(\frac{A_I - A_t}{A_I}\right) \times 100 \quad (1)$$

where C_t is the concentration at the actual measurement, and C_I is the initial concentration. Similarly, A_I and A_t are the initial and actual absorbance values, respectively.

3. Results and discussion

3.1. Structural analysis by X-ray diffraction

It is important to elucidate the crystalline nature and phase of the prepared samples using XRD. Accordingly, the structural crystallinity of single AZ (ZnO:Al), multilayer AZS (ZnO:Al/ZnS), and AZSN (ZnO:Al/ZnS/NiO) films was investigated via X-ray diffraction with 2θ (diffraction angle) scanning from 20° to 70°, as shown in Fig. 1(a). As shown in

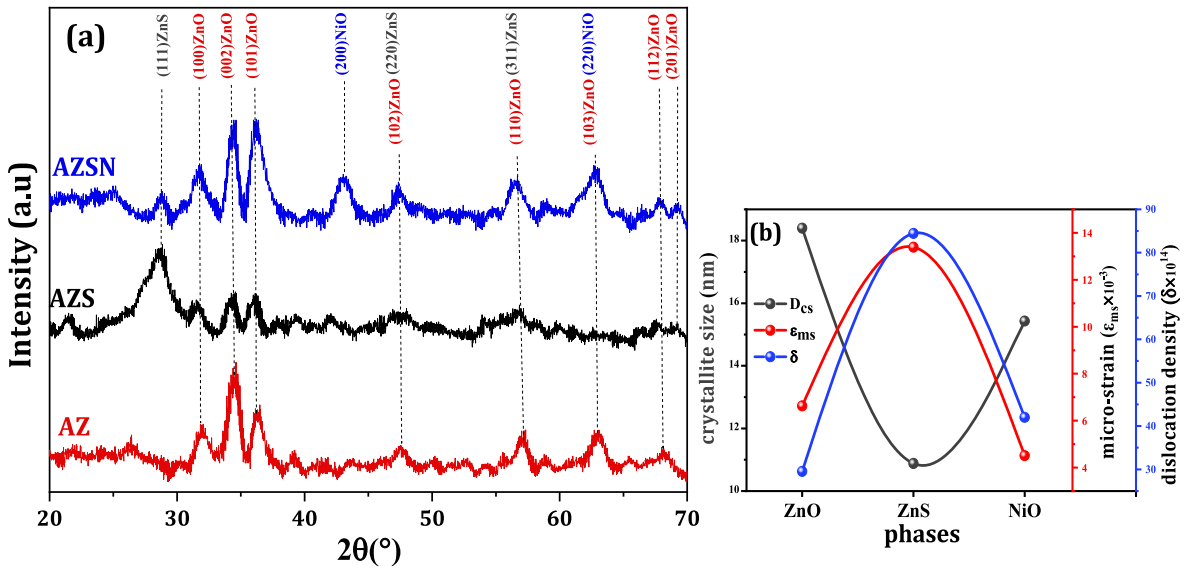

Fig. 1. a the XRD diffraction patterns of as-deposited AZ, AZS, and AZSN multilayer films, and **b** Structural parameters: crystallite size (D_{cs}), micro-strain (ε_{ms}), dislocation density (δ).

Fig. 1(a), the AZ film synthesized by the spin-coating technique showed well-defined reflections at 2θ = 31.9°, 34.5°, 36.4°, 47.6°, 56.9°, 63.0°, and 68.2° matching with (111), (002), (101), (102), (110), (103), and (112) planes, respectively, corresponding to the wurtzite hexagonal phase of ZnO (JCPDS no. 1-75-576) [38]. No aluminum-related peaks were observed in the XRD patterns (low doping concentrations in the AZ), indicating that aluminum did not change the polycrystalline wurtzite structure of ZnO.

The AZS pattern contains the most intense peak at 28.7° of the (111) plane of the zinc sulfide cubic phase (JCPDS no. 1-080-0020) [39], which is a high-intensity peak in the typical diffraction pattern of cubic ZnS with high crystallinity. Similarly, NiO traces were found in the AZSN multilayer XRD pattern with two additional peaks at 2θ = 43.2° and 62.7°, corresponding to the (200) and (220) lattice planes of the cubic phase of NiO (JCPDS no. 47-1049) [31]. Moreover, XRD confirmed the better crystalline structure of the single- and multilayer films.

The crystallite sizes (D_{cs}) of the three phases from the three samples were estimated using Debye–Scherrer's formula Eq. (2) [29]:

$$D_{cs} = \frac{0.9\lambda_{Cu}}{\beta \cos\theta} \tag{2}$$

where β is FWHM (full width at half maximum) and $\lambda_{Cu} = 0.154$ nm. D_{cs} have been used to estimate the length of dislocation lines per volume unit (dislocation density) [40] using Eq. (3).

$$\delta = \frac{1}{D_{cs}^2} \tag{3}$$

The micro-strain (ε_{ms}) is an interesting structural parameter of the deposited nanostructured thin films that originate from their structural defects it can induce the diffraction peaks broadening which is related to FWHM (β) and can be calculated using the following relation [41]:

$$\varepsilon_{ms} = \frac{\beta}{4\tan\theta} \tag{4}$$

when D_{cs} decreases, compression occurs owing to the interior surface-tension-induced lattice strain, and the number of crystal edges increases along the film surface area. Accordingly, the lattice strain becomes weak when the crystallite size increases, owing to a lower compression from the grain boundaries, and even the dislocation lines decrease because of the low number of grain boundaries, which means that the grain boundary is a trap of dislocations [40,42]. Accordingly, Fig. 1(b) displays the opposite correlation between D_{cs}, ε_{ms}, and δ for every structural phase.

All these structural parameters were calculated and are listed in Table 1.

Table 1 Structural parameters of as-deposited AZ, AZS, and AZSN films.

3.2. ATR-Fourier transform IR spectroscopy analysis

ATR-FTIR spectroscopy can be used as a supplementary analysis method for XRD studies. In this work, ATR studies were performed in the transmission mode from 400 to 4000 cm^{-1}, as shown in Fig. 2. Generally, metal oxides exhibit absorption at specific wavenumbers in the fingerprint region [30]. The AZ signal layer sample reveals the vibration of Zn–O stretching at approximately 418, 442, 459, 523, and 552 cm^{-1} [39,43–45]. The bilayer AZS thin film also showed characteristic ZnO absorption peaks at 416, 460, and 480 cm^{-1}. In addition, it reveals two other peaks assigned to the stretching vibration mode of ZnS at 555 cm^{-1} [46] and 605 cm^{-1}, which are close to the peak observed in the literature [47]. The vibration peaks of the AZSN multilayer film were located around 416, 440, and 555, and the NiO stretching mode is detected at 599 cm^{-1} [48]. For all samples, we observed broad absorption bands located around 914 and 764 cm^{-1} returning to the glass substrates [49]. Notably, the FTIR results confirmed the results of the XRD study.

3.3. Surface morphology (SEM)

The surface morphologies of the signal, bi-, and trilayer thin films were determined by SEM and are shown in Fig. 3(a–c). The SEM micrographs showed significant changes in the surface morphology according to the deposition of the upper layer. The SEM micrograph of sol-gel ZnO:Al (AZ) appears an interesting textured surface with an irregular root-like and wrinkled network structure distributed over the surface and crack-free. As can be seen from the AZ micrograph, these wrinkles have no particular or symmetrical orientations. The wrinkle-like network structure can be attributed to rapid drying after each coating layer during the deposition time. In addition, X. Li et *al.* [41] reported that slowly and quickly pre-annealed thin films exhibit smooth and wrinkled surface morphologies, respectively. Similar wrinkle-like and root-like network morphologies have been reported by other researchers

Table 1
Structural parameters of as-deposited AZ, AZS, and AZSN films.

Samples	phases	structure	2θ (°)	hkl	D_{cs} (nm)	ε_{ms} (10^{-3})	δ (10^{14} lines/m^2)	RMS
AZ	ZnO	hexagonal	31.94	100	18.4	6.63	29.54	12.07
			34.60	002				
			36.42	101				
AZS	ZnS	cubic	28.78	111	10.9	13.39	84.45	10.66
ASZN	NiO	cubic	43.14	200	15.4	4.51	42.00	21.36
			62.73	220				

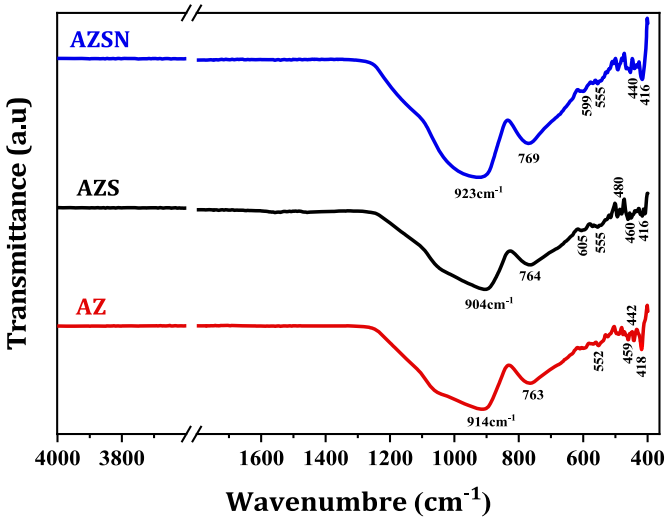

Fig. 2. ATR-FTIR spectra of as-deposited AZ, AZS, and AZSN films.

for undoped and Al-doped ZnO thin films [42,50,51] using the spin-coating method. These types of nanostructures exhibit a larger surface-to-volume ratio than that of smooth thin films. The SEM micrographs of the as-sprayed ZnS on the ZnO:Al (AZS) bilayer at different magnifications are shown in Fig. 3(b). This clearly shows that the ZnS layer owing to its good cohesion with the ZnO layer, AZS displays a smooth and dense network structure in a disk-like form with several sizes along the surface. A similar disk-like ZnS morphology was observed in Ref. [40]. A surface morphology micrograph of the NiO (upper layer of AZSN) deposited on top of the ZnS layer is shown in Fig. 3(c). Non-uniform surface structures were observed, and the sprayed NiO precursor solution exhibited low adhesion. The thin film of NiO on ZnS exhibited non-homogeneous overlapping, with nanoagglomerations of grains of various shapes and sizes. Furthermore, the void and cracked nature of the NiO film surface could be attributed to the roughness of the ZnS layer. However, the presence of nanovoids on the layer can affect its cohesion and homogeneous network structure, but it can exhibit a rough surface that facilitates dye adsorption in photocatalytic applications.

EDS was performed to confirm the chemical compositions of the AZ, AZS, and AZSN samples coated on the glass substrate, as presented in Fig. 3. To confirm the presence of the deposited element peaks in this work (Al, Zn, Ni, S, and O), which were clearly observed. Moreover, the EDS spectrum also shows the presence of (Si, O, and Ca) due to the glass substrate [42] and the Au peak originating from the Au electrical contact.

Fig. 3(a–c) also represents the direct thickness of the AZ, AZS, and AZSN obtained samples from the cross-sectional SEM images revealing an increase in thickness from mono-to multilayered films. The average thickness of each film was 736 nm, 1.3 μm, and 1.78 μm for AZ, AZS, and AZSN films, respectively.

3.4. AFM analysis and surface roughness

AFM analysis provided information about surface topography and roughness. Notably, as mentioned in the SEM, the photocatalytic performance of thin-film samples depends on their surface roughness. Fig. 4 shows the two-dimensional and three-dimensional AFM images over a 5 × 5 μm^2 scanned area. The samples exhibited different surface topographies and agglomerations of different sizes on their surfaces. Granular formations were observed on the surface of the single-layer ZnO:Al (AZ) film, unlike in other films. In fact, crystal grains can be observed, unlike the previous SEM images that displayed no defined crystal grain boundaries in the smooth or wrinkle-like zones. In addition, as shown in Fig. 4(a), the 3D topography of the AZ sample shows a granular distribution, and some agglomerations of grains grow preferentially along the c-axis and perpendicular to the film surface. The AFM and SEM results for ZnO:Al resemble are comparable to the morphology results reported by M. A. Bouacheria et *al.* [42]. The topography of the AZS sample displays agglomerates of dense grains that cover the surface (see the 3D topography in Fig. 4(b)) in a disk-like form on each other to form ellipsoidal particles of several sizes. The NiO coating film on ZnO:Al/ZnS for the trilayer AZSN sample is shown in Fig. 4(c). It displays island-like growth of grain formation, which indicates the agglomeration of nanocrystals with some voids between these agglomerated grains. The average surface root-mean-square (RMS) roughness values appreciated for all samples are listed in Table 1.

Fig. 4 The AFM images of as-deposited layers **(a)** AZ, **(b)** AZS, and **(c)** AZSN.

3.5. Optical analysis

The transmittance spectra of the films measured in the 300–800 nm wavelength range are shown in Fig. 5. The films exhibited a high transmittance in the visible region (400–700 nm). The ZnO:Al (AZ) film was highly transparent in this region, with an average optical transmittance of 85%. The above deposition of ZnS and then NiO reduced the transmittance of the film with average values of 75% and 65%, respectively. In addition, Fig. 5(a) shows a small difference between the AZ, AZS, and AZSN films on their absorption edge in the UV region, which shifts toward lower wavelengths at approximately 370 nm, this phenomenon is mostly associated with the Burstein–Moss effect [52]. The Tauc equation Eq. (5) was used to estimate the E_g of Samples [16].

$$(\alpha h\upsilon)^2 = C\left(h\upsilon - E_g\right) \tag{5}$$

where C is a constant, and hυ is the photon energy. α is calculated using the following equation [53]:

$$\alpha = 2.303\frac{Abs}{th(cm)} \tag{6}$$

where Abs is the absorbance, and th is the thickness of the layers.

Fig. 5(b) shows the Tauc plot of $(\alpha h\upsilon)^2$ vs. (hυ) in the absorption edge zone to estimate the optical gap values. From the plot, it can be observed that the bandgap values were 3.26 and 3.15 eV for AZ and AZS, respectively. The results for AZ are in agreement with those obtained by other authors [54]. ZnO:Al/ZnS (AZS) exhibits a remarkable reduction

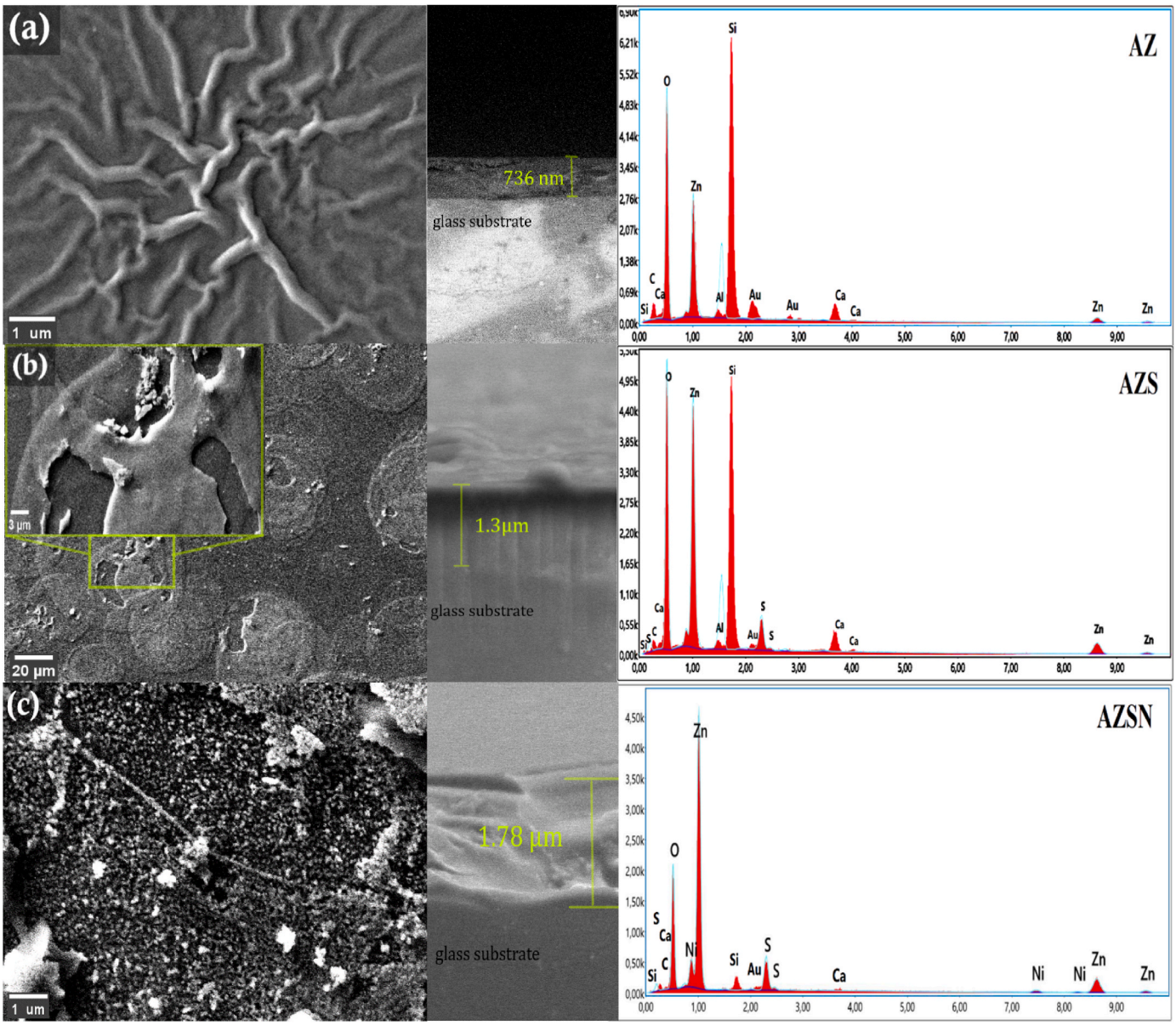

Fig. 3. SEM surface with the cross-sectional views and EDS images of as-deposited thin films **a** AZ, **b** AZS, and **c** AZSN.

in its Eg value, which is related to the addition of the ZnS phase to ZnO, resulting from a hybrid band [33]. Whereas ZnO:Al/ZnS/NiO (AZSN) exhibits in its direct band gap two absorption bands values at 3.15 eV and 3.52 eV, corresponding to the n-ZnO/n-ZnS and n-ZnS/p-NiO junctions, respectively002 E A similar Eg result for a core-shell n-ZnS/p-NiO junction has been reported in the literature [26]. This double bandgap allows for more absorption at different electromagnetic ranges.

3.6. Photocatalytic degradation

3.6.1. Mechanism of photodegradation behavior

Previous studies have always had issues with pure semiconductor thin films as photocatalysts, due to the trapping of electron-hole pairs in radiationless relaxation, which would return the semiconductor to the deactivated form even under photon energy (hυ) excitation [55], which decreases the photodegradation efficiency. Therefore, to enhance the photodegradation activity, these semiconductors should be doped with cationic or anionic dopants. Generally, dopants can occupy various sites in the lattice, such as the surface of the semiconductor, within the lattice crystal, or at interstitial sites; thus, extra energy levels appear in the bandgap. Moreover, they can couple these semiconductors with each other to create a heterojunction that plays a significant role in reducing e-h pairs through the hybrid bond that has been created [56]. In this study, ZnO:Al, ZnO:Al/ZnS, and ZnO:Al/ZnS/NiO (AZSN) thin films were tested as photocatalysts for MB under visible light. The trilayer AZSN was chosen for the rest of the study to investigate its photocatalytic activity with the pH effect (MB), stability/reusability (MB), under natural solar light against three dyes (MB, CV, and CR), as well as the photodegradation mechanism (MB). It contains a double hybrid band gap that can augment the efficiency of visible irradiation absorption for photocatalytic applications by visible/solar light illumination. The mechanism of the photocatalytic performance of AZSN as a catalyst is proposed as shown in Fig. 6(a). Under light illumination, electrons were excited to the conduction band (CB) and left holes in the valence band (VB) of NiO, ZnS, and ZnO:Al, respectively, in the AZSN trilayer thin film. The photogenerated electrons moved freely from the CB of ZnO:Al to the VB of ZnS. The electrons generated from the CB of ZnS go to the VB of NiO, resulting in the collection of electrons in the CB of NiO, whereas holes are collected in the VB of ZnO:Al in the AZSN thin film.

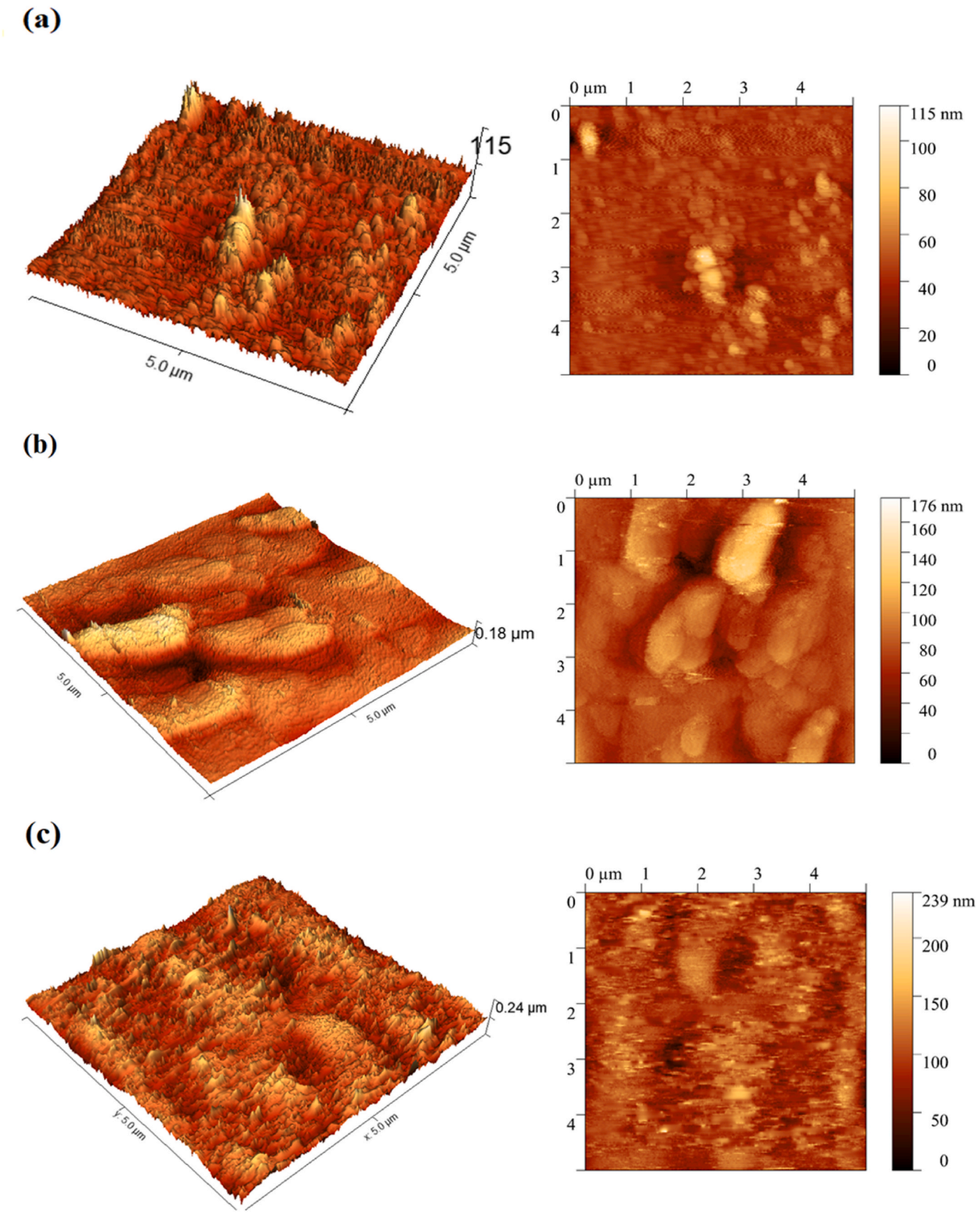

Fig. 4. The AFM images of as-deposited layers **a** AZ, **b** AZS, and **c** AZSN.

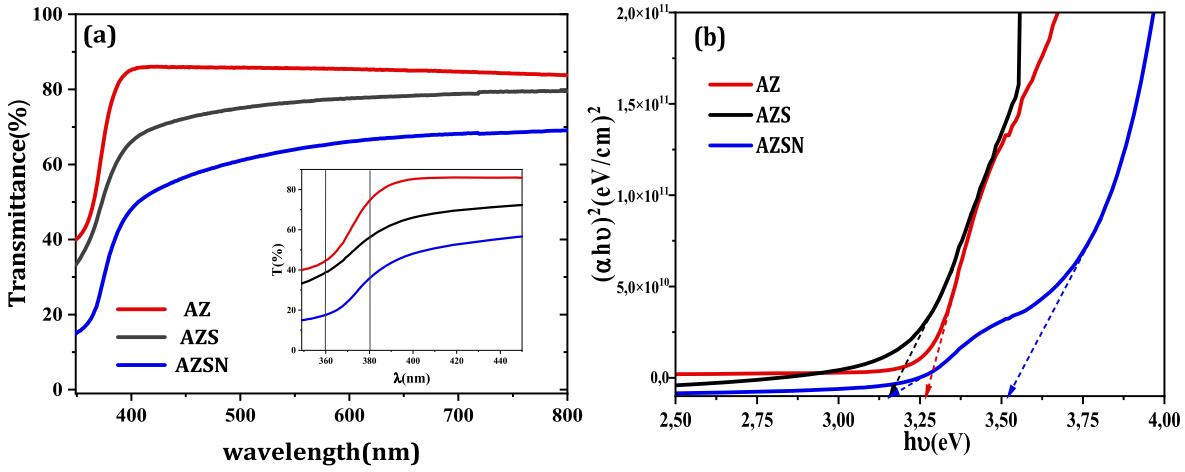

Fig. 5. a Optical transmittance spectra (Inset shows the shifting of band-edge absorption region), **b** Tauc plot of as-deposited layers AZ, AZS, and AZSN.

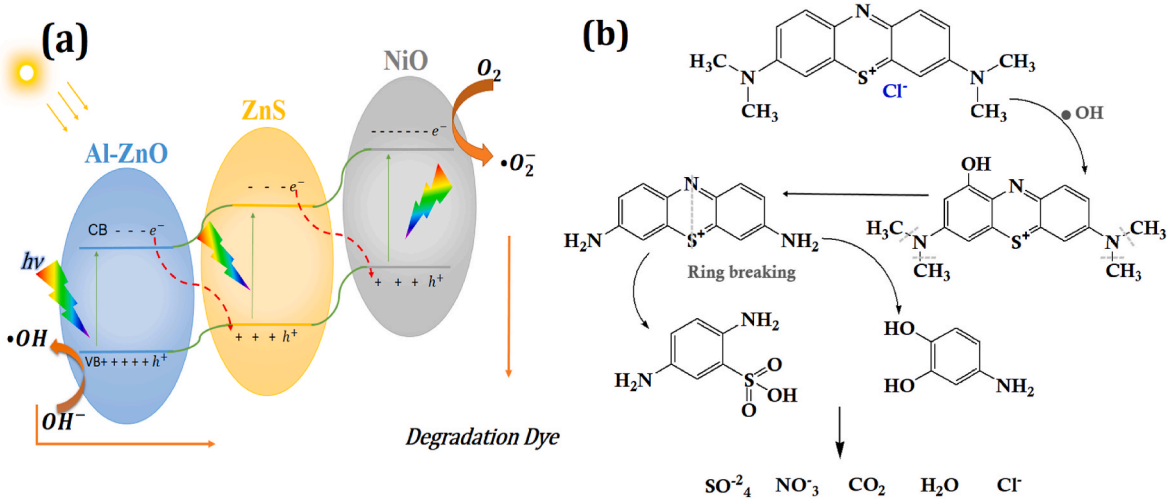

Fig. 6. a Schematic of proposed photodegradation mechanism of ASZN photocatalyst under visible illumination, **b** Suggested photocatalytic degradation steps of MB.

The electrons accumulated on the NiO surface reacted with atmospheric oxygen molecules to generate and combine superoxide ($\bullet O_2^-$) anion radicals. •OH hydroxyl radicals are generated from the oxidation of water molecules H_2O by (h^+) the accumulated holes in the VB of ZnO:Al. The resulting hydroxyl radicals as powerful oxidants, •OH and $\bullet O^{2-}$, can effectively assail environ organic molecules (dyes) and convert them to H_2O and CO_2 [35,57]. The possible mechanism of reactions of AZSN thin films on organic dyes such as MB or others under visible-light irradiation can follow the following oxidation process [34,36]:

$$Al-\mathrm{ZnO/ZnS/NiO}\xrightarrow{h\upsilon} Al-ZnO\left(e_{CB}^{-}\cdot\cdot h_{VB}^{+}\right)/ZnS\left(e_{CB}^{-}\cdot\cdot h_{VB}^{+}\right)/NiO\left(e_{CB}^{-}\cdot\cdot h_{VB}^{+}\right) \quad (7)$$

$$Al-ZnO\left(e_{CB}^{-}\cdot\cdot h_{VB}^{+}\right)/ZnS\left(e_{CB}^{-}\cdot\cdot h_{VB}^{+}\right)/NiO\left(e_{CB}^{-}\cdot\cdot h_{VB}^{+}\right)\rightarrow Al-ZnO\left(h_{VB}^{+}\right)/NiO\left(e_{CB}^{-}\right) \quad (8)$$

$$NiO\left(e_{CB}^{-}\right)+O_2\rightarrow NiO+\cdot O_2^{-} \quad (9)$$

$$Al-\mathrm{ZnO}\left(h_{VB}^{+}\right)+H_2O\rightarrow H^{+}+\cdot OH \quad (10)$$

$$\cdot OH+dye\rightarrow Degraded\ products. \quad (11)$$

For better understanding, a detailed description of the probable photocatalytic degradation steps of Methylene Blue generated at the photocatalysis operation time is presented in Fig. 6(b). Previous studies concluded that Cl−ions can be ionized during the dissolution of MB in water [58]. Initially, a hydroxylated OH–MB compound can be formed. During the photocatalytic process, the MB molecules are weakened by •OH radicals in the subsequent reaction step via demethylation by attacking the N–CH_3 bond to form CH_2O + H_2, followed by the production of CO_2 and H_2O in the oxidation processes [59]. Additionally, •OH radicals can break the C–S+=C bond, resulting in a C–S(=O)–C bond [59], necessitating the breaking of the central ring with S and N heteroatoms. The nitrogen groups are exchanged by •OH radicals to liberate the NH_2 radical, which generates NH_4^+ cations that are later oxidized into NO_3^- ions [60]. Simultaneously, sulfur is hydrolyzed,

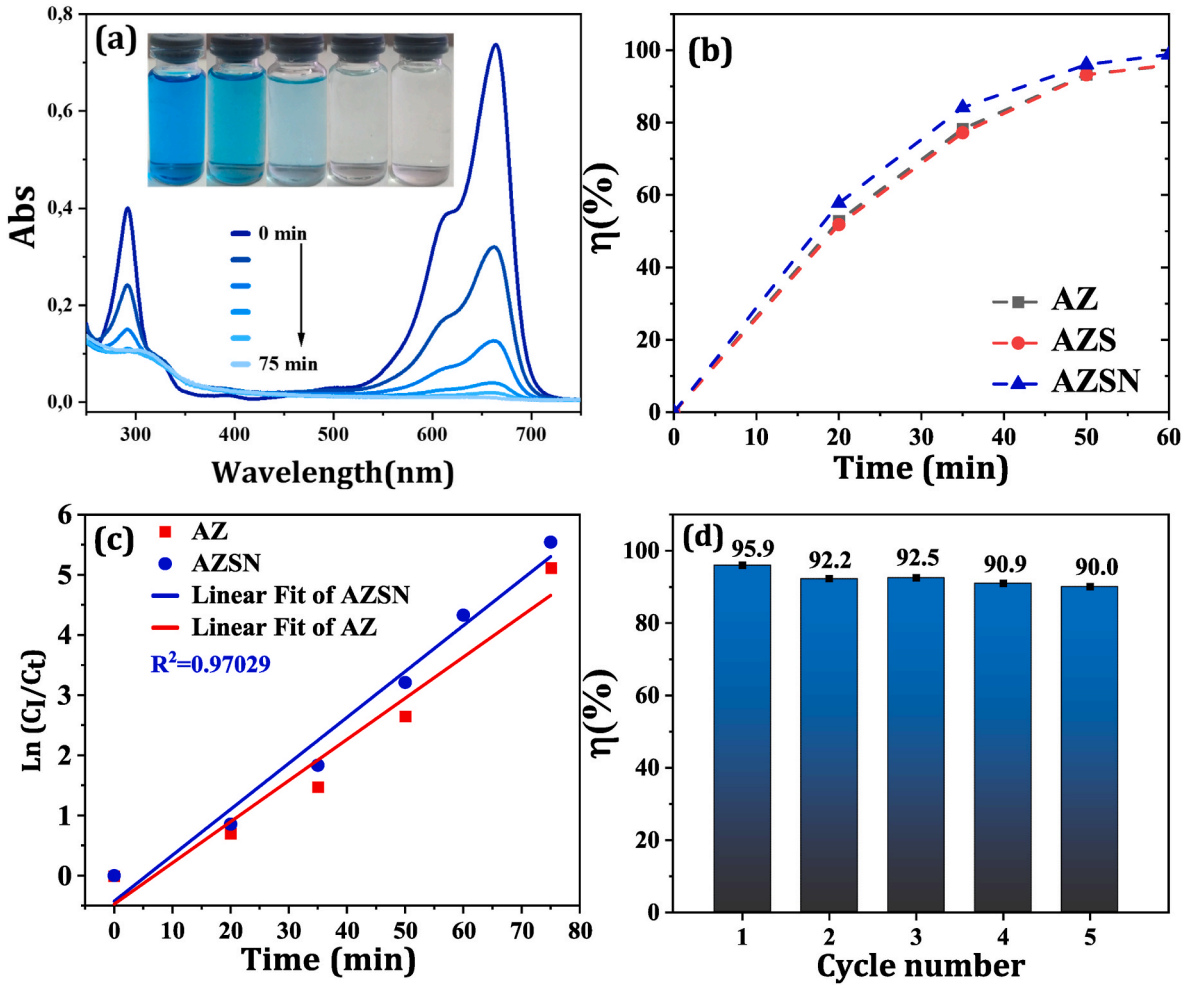

Fig. 7. a UV–visible spectra of MB solution under halogen lamp illumination using an AZSN as a catalyst, **b** Photodegradation rate curves of MB under visible light using AZ, AZS, and AZSN as catalysts, **c** Kinetics of the MB dye photodegradation catalyzed by AZ and AZSN, and **d** Recyclability of AZSN photocatalyst with MB under visible illumination.

oxidized, and converted into SO_4^{2-}. The MB organic dye degraded into small species such as CO_2 and water and mineralized into inorganic products such as SO_4^{2-} and NO_3^- ions.

Fig. 6 a Schematic of proposed photodegradation mechanism of ASZN photocatalyst under visible illumination, and **b** Suggested photocatalytic degradation steps of MB.

3.6.2. *Photocatalytic degradation under visible irradiation*

To investigate the photodegradation activities of the single-, bilayer-, and trilayer heterostructure films, an aqueous MB solution was chosen as the organic pollutant. The evolution of the dye was measured by UV–vis absorption at the absorbance maximum during the process, as shown in Fig. 7(a). The main absorption peak was located at $\lambda_{max} = 664$ nm, corresponding to MB molecules. The MB degradation rate increased with the exposure time of visible light irradiation, and after 50 min, it almost completely disappeared with a photocatalytic degradation efficiency (η%) of ~96% for AZSN, and the degradation reached 93% for the AZ and AZS samples. The degradation efficiency of AZSN catalyst increased to 99.81% after 75 min. Fig. 7(b) shows that all the samples exhibited excellent efficiency. However, AZSN was chosen for the rest of the photocatalytic investigation because ZnO:Al and ZnO:Al/ZnS samples have been investigated in previous studies [27,36,37]. In addition, AZSN exhibited the highest photocatalytic performance.

The photodegradation kinetic rate constant (k) of MB dye was estimated from the slopes of the plots of ln (C_I/C_t) vs. time of irradiation (Fig. 7(c)), using the first-order model from Eq. (12) [20]:

$$ln\frac{C_I}{C_t} = kt \tag{12}$$

where C_I, C_t, and k are the initial concentration, the concentration of the dye during the process, and the rate constant, respectively. k values were found to be 0.06844 min^{-1} for the AZ and 0.07638 min^{-1} for AZSN with correlation coefficients R^2~0.94 and 0.97 for AZ and AZSN, respectively. Higher R^2 and k degradation rates obtained were for the AZSN trilayer thin film, confirming its superior decolorization ability.

Fig. 7(d) illustrates the stability and reusability of the AZSN catalyst for MB degradation under visible irradiation for 50 min. The experiment was performed five times with a small reduction in the photocatalytic performance, with almost 90% decomposition after the 5th process. This clearly shows that the photodegradation of MB was slightly reduced (~6%), which is believed to provide long-term stability in real time for practical industrial photocatalytic applications. Thus, the investigated AZSN photocatalyst sample exhibited a high MB stability.

3.6.3. *Effect of pH*

Solution pH plays an important role in the photocatalytic process [61] because it controls the reactions during the decolorization of organic dyes [62]. Optimization of the pH is necessary to achieve optimum degradation efficiency. To evaluate the effect of pH on dye degradation, all experiments were carried out using the AZSN film catalyst for 60 min under visible light irradiation. The pH values were

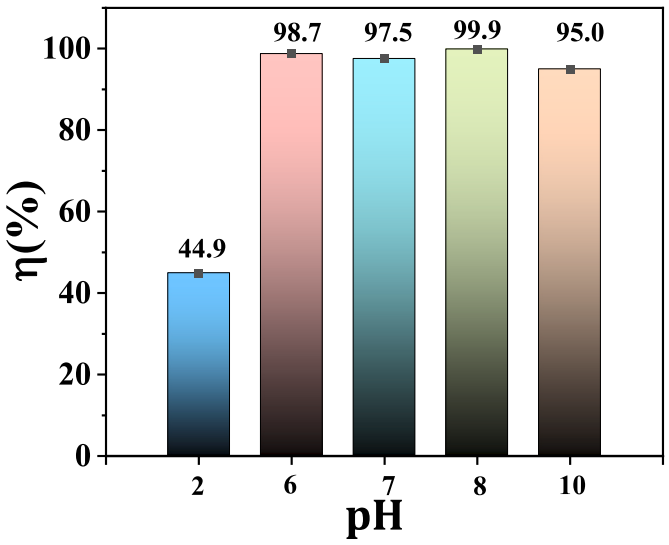

Fig. 8. The rate degradation of different pH values of MB with AZSN catalyst.

adjusted using NaOH and HCl, as shown in Fig. 8. This clearly shows that the dye discoloration was lower at lower pH values. When the pH of the MB aqueous solution was increased from 6, the photodegradation efficiency of the AZSN catalyst increased. In the pH range of 6–10 the value of MB degradation was higher than that at acidic pH = 2 under visible irradiation. Compared to the basic, neutral, and acidic regions, the sample exhibited better photodegradation activity in the neutral and alkaline regions. This may be attributed to the greater availability of OH^- ions compared to the acidic medium as well as the production of more OH radicals by combining with holes (h^+) generated by the electronic (e^-) catalyst excited by irradiation. Furthermore, this may be associated with the cationic nature of the MB dye solution [63].

3.6.4. *Photocatalytic degradation under natural solar light irradiation*

In the second photocatalytic process step, MB, CV, and CR dyes were selected as targets to assess their photocatalytic degradation ability under natural sunlight irradiation. In addition, the maximum absorbance of the dyes was scanned in the visible range (300–800 nm), as shown in Fig. 9 (e), it was at λ = 664, 583, and 498 nm, ascribed to the MB, CV, and CR organic dyes, respectively. Changes in the maximum absorbance were observed in order to estimate the photocatalytic degradation rate. The same conditions were used in the first step of the photocatalytic experiments under visible light. Fig. 9(a–c) show the UV–vis spectra and photodegradation rate (Fig. 9(d)) of the three dyes: MB, CV, and CR. The absorption peaks at λ_{max} for the three organic dyes gradually decrease with time. It observed when the illumination time

Table 2
degradation efficiency (η), reaction time, rate constant (k), and R2 values of AZ, AZS, and AZSN for the organic dyes under light irradiation.

Sample	organic dye	irradiation type	rate constant, K (min^{-1})	R^2 value	η(%)	time (min)
AZSN	MB	Visible	0.07638	0.97	95.99	**50**
AZ	MB	Visible	0.06844	0.93	93.26	**50**
AZS	MB	Visible	0.05230	0.94	93.16	**50**
AZSN	MB	sunlight	0.02588	0.98	90.12	**90**
AZSN	CV	sunlight	0.01057	0.96	85.48	**90**
AZSN	CR	sunlight	0.00425	0.63	65.42	**90**

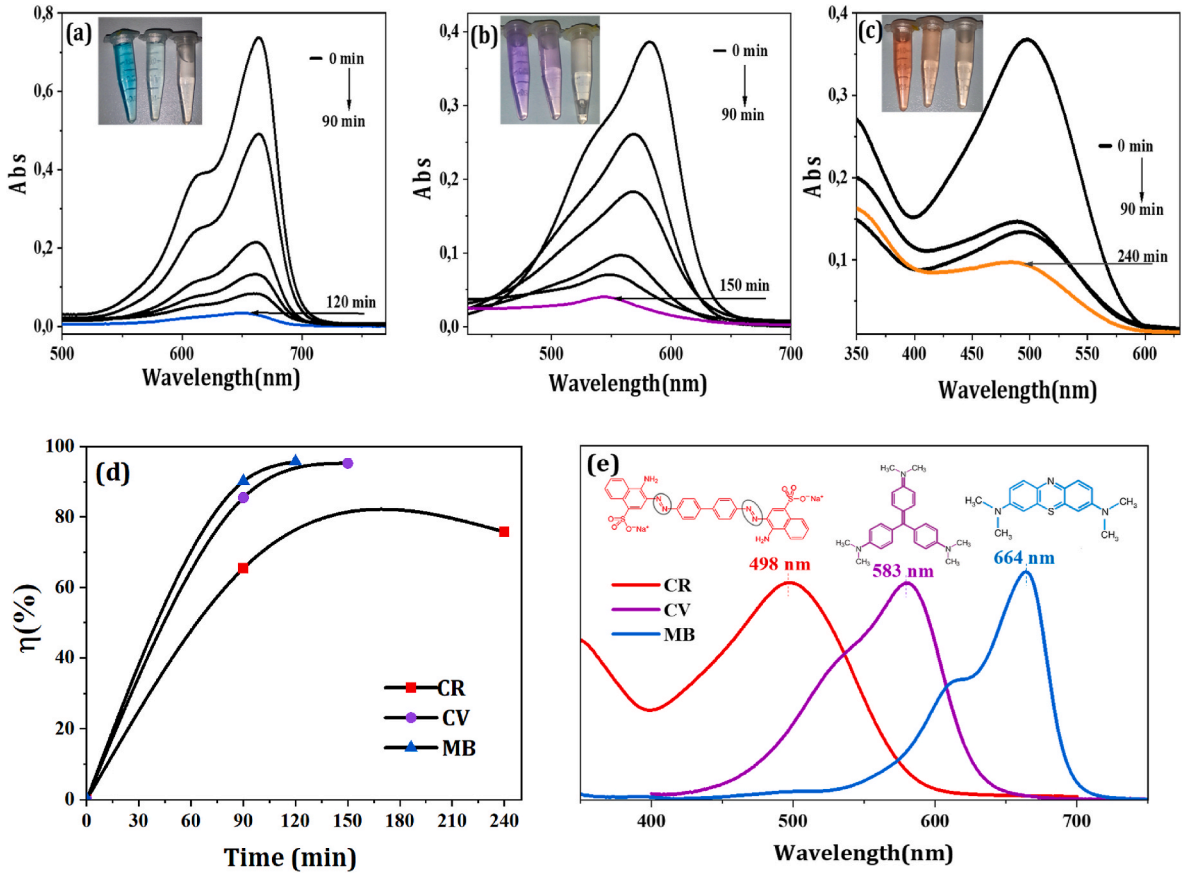

Fig. 9. a–c UV–visible spectra rate curves under sunlight irradiation of **a** MB, **b** CV, and **c** CR using AZSN as catalysts, **d** Degradation efficiency of dyes (MB, CV, and CR) under sunlight irradiation using AZSN as a catalyst, and **e** UV–Vis spectra of MB, CV, and CR.

was 90 min under sunlight irradiation, the photocatalytic decomposition rates were 90%, 85%, and 65% for MB, CV, and CR, respectively, and it was 83% for MB over just 60 min. CR is a difficult decolorized dye compared to MB or CV. This can be attributed to the presence of many benzene rings in their structure and the presence of two azo bonds, N=N, which have a high bond energy of 4.33 eV [20,59]. Similarly, this can explain the photodegradation efficiency of only 75.76% over 4 h of exposure to sunlight irradiation, which was very slow compared to 1.5h of $\eta = 65\%$. Even the first-order kinetic value (k) of CR was 0.00425 min^{-1} with a small correlation coefficient ($R^2 = 0.63$), which was the lowest value in this case. The kinetic rate (K) and R^2 values are listed in Table 2.

Table 2% degradation efficiency (η), reaction time, rate constant (k), and R2 values of AZ, AZS, and AZSN for the organic dyes under light irradiation.

Fig. 9 a-c UV–visible spectra rate curves under sunlight irradiation of **a** MB, **b** CV, and **c** CR using AZSN as catalysts, **d** Degradation efficiency of dyes (MB, CV, and CR) under sunlight irradiation using AZSN as a catalyst, and **e** UV–Vis spectra of MB, CV, and CR.

4. Conclusion

This study demonstrated a simple cost-effective spin coating (sol-gel) and spray pyrolysis method to synthesize Al-doped ZnO, which was then coated with ZnS and NiO, respectively, as upper layers. XRD and supplemental FTIR analyses confirmed the successful preparation, revealing the existence of only ZnO, ZnS, and NiO phases. Morphological SEM analysis indicated that the deposition of different nanocrystalline films above one another could deteriorate the adherence of the upper layer, which can influence its homogenous shapes. AFM analysis of the films showed acceptable surface roughness for the photocatalyst samples, making it larger than the smoothed volume ratio. The EDS mapping analysis demonstrated the existence of an Al trace in the sample. The optical characteristics of thin films have been reported that the E_g value of ZnO:Al monolayer of 3.26 eV is decreased to 3.15 eV after Al–ZnO/ZnS coupling, whereas the trilayer ZnO:Al/ZnS/NiO exhibits an additional absorption value of 3.52 eV due to the NiO layer. The results indicate that ZnO:Al/ZnS/NiO exhibits a high photodegradation efficiency (~96%) against MB within 50 min under visible light, improving its stability and reusability in real time in industrial applications, with a very slight reduction observed after the fifth cycle. Furthermore, when we replaced visible light source with solar radiation, which is a free renewable source of energy, the catalytic photodegradation activities of ZnO:Al/ZnS/NiO for 90 min showed degradation rates of 90%, 85%, and 65% against MB, CV, and CR, respectively. This work is suggested to open the door for cost-effective synthesis of doped and coupled multilayer thin films to obtain more absorption bands, rough, and stable photocatalyst properties for efficient water treatment applications using plentiful sunlight.

Credit author statement

S. Besra: Planning of the experiments, Sample preparation, Characterization, Formal analysis, and interpretation and Manuscript writing. K. Belakroum: Writing- Reviewing and Editing. S. Iaiche: Writing-Reviewing and Editing. D. Aouf: Planning of the experiments, Writing-Original draft preparation. Y. Rahmani: Formal analysis, Planning of the experiments, and interpretation. D. Zerrouki: Writing- Reviewing and Editing. H. Belkhalfa: Writing- Reviewing and Editing. A. Henni: Conceptualization of the ideas, Reviewing and Manuscript Editing.

Declaration of competing interest

The authors declare that they have no known competing financial interests or personal relationships that could have appeared to influence the work reported in this paper.

Data availability

No data was used for the research described in the article.

References

[1] R.S. Pedanekar, S.K. Shaikh, K.Y. Rajpure, Thin film photocatalysis for environmental remediation: a status review, Curr. Appl. Phys. 20 (2020) 931–952, https://doi.org/10.1016/j.cap.2020.04.006.
[2] A. Arfaoui, A. Mhamdi, Physical investigations and photocatalytic activity test of NiMoO4 thin films prepared by spray pyrolysis technique, Bull. Mater. Sci. 45 (2022), https://doi.org/10.1007/s12034-022-02723-3.
[3] M. Adeel, M. Saeed, I. Khan, M. Muneer, N. Akram, Synthesis and characterization of Co-ZnO and evaluation of its photocatalytic activity for photodegradation of methyl orange, ACS Omega 6 (2021) 1426–1435, https://doi.org/10.1021/acsomega.0c05092.
[4] V. Navakoteswara Rao, P. Ravi, M. Sathish, N. Lakshmana Reddy, K. Lee, M. Sakar, P. Prathap, M. Mamatha Kumari, K. Raghava Reddy, M.N. Nadagouda, T. M. Aminabhavi, M.V. Shankar, Monodispersed core/shell nanospheres of ZnS/NiO with enhanced H2 generation and quantum efficiency at versatile photocatalytic conditions, J. Hazard Mater. 413 (2021), https://doi.org/10.1016/j.jhazmat.2021.125359.
[5] M.R. Khanlary, S. Tarzi, Study of structural, optical and morphological properties of ZnO/ZnS hetrostructures deposited by spray pyrolysis method, Opt. Quant. Electron. 53 (2021) 1–10, https://doi.org/10.1007/s11082-020-02657-2.
[6] M. Salah, W. Zayani, B. Bouricha, S. Azizi, A. Alatrache, M. Amlouk, J. Lamloumi, Vibrational study of Li-doped ZnO sprayed thin films along with sensors under ethanol vapor and photocatalytic applications, J. Mater. Sci. Mater. Electron. 31 (2020) 18883–18902, https://doi.org/10.1007/s10854-020-04426-z.
[7] D. Saravanakkumar, S. Sivaranjani, K. Kaviyarasu, A. Ayeshamariam, B. Ravikumar, S. Pandiarajan, C. Veeralakshmi, M. Jayachandran, M. Maaza, Synthesis and characterization of ZnO-CuO nanocomposites powder by modified perfume spray pyrolysis method and its antimicrobial investigation, J. Semicond. 39 (2018), https://doi.org/10.1088/1674-4926/39/3/033001.
[8] N. Talebian, M. Doudi, H. Mogoei, Antibacterial activities of sol–gel derived ZnO-multilayered thin films: p-NiO heterojunction layer effect, J. Sol. Gel Sci. Technol. 74 (2015) 650–660, https://doi.org/10.1007/s10971-015-3644-1.
[9] M. Baradaran, F.E. Ghodsi, C. Bittencourt, E. Llobet, The role of Al concentration on improving the photocatalytic performance of nanostructured ZnO/ZnO:Al/ZnO multilayer thin films, J. Alloys Compd. 788 (2019) 289–301, https://doi.org/10.1016/j.jallcom.2019.02.184.
[10] M. Baradaran, F.E. Ghodsi, Highly efficient visible photocatalytic degradation of MB organic dye by heteromorphic ZnO/AZO/ZnO nanocatalysts: effect of AZO thickness, J. Sol. Gel Sci. Technol. 92 (2019) 25–39, https://doi.org/10.1007/s10971-019-05081-5.
[11] M.A.M. Ahmed, W.E. Meyer, J.M. Nel, Effect of (Ce, Al) co-doped ZnO thin films on the Schottky diode properties fabricated using the sol-gel spin coating, Mater. Sci. Semicond. Process. 103 (2019), https://doi.org/10.1016/j.mssp.2019.104612.
[12] R. Barir, B. Benhaoua, S. Benhamida, A. Rahal, T. Sahraoui, R. Gheriani, Effect of precursor concentration on structural optical and electrical properties of NiO thin films prepared by spray pyrolysis, J. Nanomater. 2017 (2017), https://doi.org/10.1155/2017/5204639.
[13] O.A. Ali, M.A. Hameed, Q.G. Al-Zaidi, Electrical properties of pure NiO and NiO:Ag thin films prepared by pulsed laser deposition, Trans. Indian Natl. Acad. Eng. 5 (2020) 27–31, https://doi.org/10.1007/s41403-020-00086-x.
[14] D. Aouf, A. Henni, D. Selloum, Y. Khane, F. Fenniche, D. Zerrouki, H. Belkhalfa, N. Dizge, Facile preparation and characterization of nanostructured ZnS/PbS heterojunction thin films for enhanced microbial inhibition and photocatalytic degradation, Mater. Chem. Phys. 295 (2023), 127059, https://doi.org/10.1016/j.matchemphys.2022.127059.
[15] G.Y. Shaikh, D.S. Nilegave, S.S. Girawale, K.B. Kore, S.R. Newaskar, S.A. Sahu, A. M. Funde, Structural, optical, photoelectrochemical, and electronic properties of the photocathode CuS and the efficient CuS/CdS heterojunction, ACS Omega 7 (2022) 30233–30240, https://doi.org/10.1021/acsomega.2c03352.
[16] H. Benamra, H. Saidi, A. Attaf, M.S. Aida, A. Derbali, N. Attaf, Physical properties of Al-doped ZnS thin films prepared by ultrasonic spray technique, Surface. Interfac. 21 (2020), https://doi.org/10.1016/j.surfin.2020.100645.
[17] A. Abdel-Kader, F.J. Bryant, Blue light emitting ZnS diodes, J. Mater. Sci. 21 (1986) 3227–3230, https://doi.org/10.1007/BF00553360.
[18] A. Attaf, A. Derbali, H. Saidi, H. Benamra, M.S. Aida, N. Attaf, H. Ezzaouia, L. Derbali, Physical properties of Pb doped ZnS thin films prepared by ultrasonic spray technique, Phys. Lett. Sect. A Gen. At. Solid State Phys. 384 (2020), 126199, https://doi.org/10.1016/j.physleta.2019.126199.
[19] A. Derbali, A. Attaf, H. Saidi, M.S. Aida, H. Benamra, R. Attaf, N. Attaf, H. Ezzaouia, L. Derbali, Br doping effect on structural, optical and electrical properties of ZnS thin films deposited by ultrasonic spray, Mater. Sci. Eng. B Solid-State Mater. Adv. Technol. 268 (2021), 115135, https://doi.org/10.1016/j.mseb.2021.115135.
[20] F.Z. Nouasria, D. Selloum, A. Henni, S. Tingry, J. Hrbac, Improvement of the photocatalytic performance of ZnO thin films in the UV and sunlight range by Cu doping and additional coupling with Cu2O, Ceram. Int. 48 (2022) 13283–13294, https://doi.org/10.1016/j.ceramint.2022.01.207.

[21] M.A. Ciolan, I. Motrescu, Pulsed laser ablation: a facile and low-temperature fabrication of highly oriented n-type zinc oxide thin films, Appl. Sci. 12 (2022), https://doi.org/10.3390/app12020917.
[22] R. Singh, M. Gupta, S.K. Mukherjee, Effect of Ag layer thickness on optical and electrical properties of ion-beam-sputtered TiO2/Ag/TiO2 multilayer thin film, J. Mater. Sci. Mater. Electron. 33 (2022) 6942–6953, https://doi.org/10.1007/s10854-022-07873-y.
[23] Y. Bouznit, A. Henni, Enhanced photoelectrochemical performance of Al-doped ZnO thin films prepared by co-spray technique, Mater. Sci. Semicond. Process. 118 (2020), 105208, https://doi.org/10.1016/j.mssp.2020.105208.
[24] S. Iaiche, C. Boukaous, D. Alamarguy, A. Djelloul, D. Hamana, Effect of solution concentration on ZnO/ZnAl2O4 nanocomposite thin films formation deposited by ultrasonic spray pyrolysis on glass and si(111) substrates, J. Nano Res. 63 (2020) 10–30. https://10.4028/www.scientific.net/JNanoR.63.10.
[25] H.W. Wu, C.H. Chu, Structural and optoelectronic properties of AZO/Mo/AZO thin films prepared by rf magnetron sputtering, Mater, Lett 105 (2013) 65–67, https://doi.org/10.1016/j.matlet.2013.04.017.
[26] V. Navakoteswara Rao, V. Preethi, U. Bhargav, P. Ravi, A. Kumar, M. Sathish, V. Krishnan, V. Venkatramu, M. Mamatha Kumari, K.R. Reddy, N.P. Shetti, T. M. Aminabhavi, M.V. Shankar, Gram-scale synthesis of ZnS/NiO core-shell hierarchical nanostructures and their enhanced H2 production in crude glycerol and sulphide wastewater, Environ. Res. 199 (2021), https://doi.org/10.1016/j.envres.2021.111323.
[27] M.R. Islam, M. Rahman, S.F.U. Farhad, J. Podder, Structural, optical and photocatalysis properties of sol–gel deposited Al-doped ZnO thin films, Surface. Interfac. 16 (2019) 120–126, https://doi.org/10.1016/j.surfin.2019.05.007.
[28] X. Zhang, J. Qin, Y. Xue, P. Yu, B. Zhang, L. Wang, R. Liu, Effect of aspect ratio and surface defects on the photocatalytic activity of ZnO nanorods, Sci. Rep. 4 (2014) 4–11, https://doi.org/10.1038/srep04596.
[29] B. Al Farsi, F. Al Marzouqi, M. Al-Maashani, M.T. Souier, M. Tay Zar Myint, M. Z. Al-Abri, Rapid microwave-assisted fabrication of Al-doped zinc oxide nanorods on a glass substrate for photocatalytic degradation of phenol under visible light irradiation, Mater. Sci. Eng. B Solid-State Mater. Adv. Technol. 264 (2021), https://doi.org/10.1016/j.mseb.2020.114977.
[30] S. Ben Ameur, H. BelHadjltaief, B. Duponchel, G. Leroy, M. Amlouk, H. Guermazi, S. Guermazi, Enhanced photocatalytic activity against crystal violet dye of Co and in doped ZnO thin films grown on PEI flexible substrate under UV and sunlight irradiations, Heliyon 5 (2019), https://doi.org/10.1016/j.heliyon.2019.e01912.
[31] S.C. Bulakhe, R.J. Deokate, Electrochemically prepared Fe: NiO thin film catalysis for oxygen evolution reaction, J. Mater. Sci. Mater. Electron. 33 (2022) 18180–18186, https://doi.org/10.1007/s10854-022-08674-z.
[32] T. Munawar, M.S. Nadeem, F. Mukhtar, M. Hasan, K. Mahmood, M.I. Arshad, A. Hussain, A. Ali, M.S. Saif, F. Iqbal, Rare earth metal co-doped Zn0·9La0.05M0.05O (M = Yb, Sm, Nd) nanocrystals; energy gap tailoring, structural, photocatalytic and antibacterial studies, Mater. Sci. Semicond. Process. 122 (2021), https://doi.org/10.1016/j.mssp.2020.105485.
[33] Z. Ren, X. Li, L. Guo, J. Wu, Y. Li, W. Liu, P. Li, Y. Fu, J. Ma, Facile synthesis of ZnO/ZnS heterojunction nanoarrays for enhanced piezo-photocatalytic performance, Mater. Lett. 292 (2021), https://doi.org/10.1016/j.matlet.2021.129635.
[34] N. Paul Talinungsang, D. Dhar Purkayastha, M.G. Krishna, TiO 2/SnO 2 and SnO 2/TiO 2 heterostructures as photocatalysts for degradation of stearic acid and methylene blue under UV irradiation, Superlattices Microstruct 129 (2019) 105–114, https://doi.org/10.1016/j.spmi.2019.03.004.
[35] S. Chen, F. Liu, M. Xu, J. Yan, F. Zhang, W. Zhao, Z. Zhang, Z. Deng, J. Yun, R. Chen, C. Liu, First-principles calculations and experimental investigation on SnO2@ZnO heterojunction photocatalyst with enhanced photocatalytic performance, J. Colloid Interface Sci. 553 (2019) 613–621, https://doi.org/10.1016/j.jcis.2019.06.053.
[36] B. Al Farsi, T.M. Souier, F. Al Marzouqi, M. Al Maashani, M. Bououdina, H. M. Widatallah, M. Al Abri, Structural and optical properties of visible active photocatalytic Al doped ZnO nanostructured thin films prepared by dip coating, Opt. Mater. 113 (2021), https://doi.org/10.1016/j.optmat.2021.110868.
[37] U.P.S. Gahlaut, V. Kumar, Y.C. Goswami, Enhanced photocatalytic activity of low cost synthesized Al doped amorphous ZnO/ZnS heterostructures, Phys. E Low-Dimensional Syst. Nanostructures. 117 (2020) 1–6, https://doi.org/10.1016/j.physe.2019.113792.
[38] F. Eskandari, M. Ranjbar, P. Kameli, H. Salamati, Laser induced photoconductivity in sol-gel derived Al doped ZnO thin films, J. Alloys Compd. 649 (2015) 35–45, https://doi.org/10.1016/j.jallcom.2015.07.093.
[39] A. Baranowska-Korczyc, M. Kościński, E.L. Coy, B.F. Grześkowiak, M. Jasiurkowska-Delaporte, B. Peplińska, S. Jurga, ZnS coating for enhanced environmental stability and improved properties of ZnO thin films, RSC Adv. 8 (2018) 24411–24421, https://doi.org/10.1039/c8ra02823k.
[40] A. Derbali, H. Saidi, A. Attaf, H. Benamra, A. Bouhdjer, N. Attaf, H. Ezzaouia, L. Derbali, M.S. Aida, Solution flow rate influence on ZnS thin films properties grown by ultrasonic spray for optoelectronic application, J. Semicond. 39 (2018) 1–7, https://doi.org/10.1088/1674-4926/39/9/093001.
[41] X. Li, X. Zhu, D. Yang, Enhanced luminescent performance with surface wrinkled Al-doped ZnO films, J. Mater. Sci. Mater. Electron. 31 (2020) 6304–6312, https://doi.org/10.1007/s10854-020-03186-0.
[42] M.A. Bouacheria, A. Djelloul, M. Adnane, Y. Larbah, L. Benharrat, Characterization of pure and Al doped ZnO thin films prepared by sol gel method for solar cell applications, J. Inorg. Organomet. Polym. Mater. 32 (2022) 2737–2747, https://doi.org/10.1007/s10904-022-02313-0.
[43] N.P. Poddar, S.K. Mukherjee, Investigations on preferentially oriented Al-doped ZnO films developed using rf magnetron sputtering, J. Mater. Sci. Mater. Electron. 30 (2019) 537–548, https://doi.org/10.1007/s10854-018-0320-6.
[44] D. Djouadi, A. Chelouche, A. Aksas, Amplification of the UV emission of ZnO: Al thin films prepared by sol-gel method, J. Mater. Environ. Sci. 3 (2012) 585–590.
[45] M. Sypniewska, R. Szczesny, P. Popielarski, K. Strzalkowski, B. Derkowska-Zielinska, Structural, morphological and photoluminescent properties of annealed ZnO thin layers obtained by the rapid sol-gel spin-coating method, Opto-Electron. Rev. 28 (2020) 182–190, https://doi.org/10.24425/opelre.2020.134460.
[46] M. Nikzad, M.R. Khanlary, S. Rafiee, Structural, optical and morphological properties of Cu-doped ZnS thin films synthesized by sol–gel method, Appl. Phys. Mater. Sci. Process 125 (2019) 1–9, https://doi.org/10.1007/s00339-019-2790-7.
[47] A. Tounsi, R. Khalfi, D. Talantikite-Touati, H. Merzouk, A. Souici, Characterization of cerium-doped zinc sulfide thin films synthesized by sol–gel method, Appl. Phys. Mater. Sci. Process 128 (2022), https://doi.org/10.1007/s00339-022-05409-z.
[48] E.E. El-Katori, E.A. Kasim, D.A. Ali, Sol–gel synthesis of mesoporous NiO/ZnO heterostructure nanocomposite for photocatalytic and anticorrosive applications in aqueous media, Colloids Surfaces A Physicochem. Eng. Asp. 636 (2022), https://doi.org/10.1016/j.colsurfa.2021.128153.
[49] E. György, A. Pérez del Pino, J. Roqueta, C. Sánchez, A.G. Oliva, Processing and immobilization of chondroitin-4-sulphate by UV laser radiation, Colloids Surf. B Biointerfaces 104 (2013) 169–173, https://doi.org/10.1016/j.colsurfb.2012.11.044.
[50] H. Sutanto, S. Durri, S. Wibowo, H. Hadiyanto, E. Hidayanto, Rootlike morphology of ZnO:Al thin film deposited on amorphous glass substrate by sol-gel method, Phys. Res. Int. 2016 (2016), https://doi.org/10.1155/2016/4749587.
[51] T. Ivanova, A. Harizanova, T. Koutzarova, B. Vertruyen, R. Closset, Structural and optical characterization of nitrogen and gallium co-doped ZnO thin films, deposited by sol-gel method, J. Mol. Struct. 1206 (2020), 127773, https://doi.org/10.1016/j.molstruc.2020.127773.
[52] D. Fang, K. Lin, T. Xue, C. Cui, X. Chen, P. Yao, H. Li, Influence of Al doping on structural and optical properties of Mg-Al co-doped ZnO thin films prepared by sol-gel method, J. Alloys Compd. 589 (2014) 346–352, https://doi.org/10.1016/j.jallcom.2013.11.061.
[53] A. Najim, B. Hartiti, H. Labrim, S. Fadili, M. Ertuğrul, P. Thevenin, Synthesis of ZnS thin films using the spray pyrolysis technique, J. Mater. Sci. Mater. Electron. 33 (2022) 15086–15097, https://doi.org/10.1007/s10854-022-08428-x.
[54] H. Layoul, F. Meriche, Y. Bouznit, A. Boukerika, Structural and optical characterization of sol–gel processed Al-doped ZnO waveguide films for integrated optical devices, Appl. Phys. Mater. Sci. Process 127 (2021) 1–12, https://doi.org/10.1007/s00339-021-04752-x.
[55] M.I. Din, J. Najeeb, G. Ahmad, Recent advancements in the architecting schemes of zinc oxide-based photocatalytic assemblies, Sep. Purif. Rev. 47 (2018) 267–287, https://doi.org/10.1080/15422119.2017.1383918.
[56] H. Wang, L. Zhang, Z. Chen, J. Hu, S. Li, Z. Wang, J. Liu, X. Wang, Semiconductor heterojunction photocatalysts: design, construction, and photocatalytic performances, Chem. Soc. Rev. 43 (2014) 5234–5244, https://doi.org/10.1039/c4cs00126e.
[57] R. Mahdavi, S.S.A. Talesh, Sol-gel synthesis, structural and enhanced photocatalytic performance of Al doped ZnO nanoparticles, Adv. Powder Technol. 28 (2017) 1418–1425, https://doi.org/10.1016/j.apt.2017.03.014.
[58] I. Khan, K. Saeed, I. Zekker, B. Zhang, A.H. Hendi, A. Ahmad, S. Ahmad, N. Zada, H. Ahmad, L.A. Shah, T. Shah, I. Khan, *Water* 14.2 (2022) 242, https://doi.org/10.3390/w14020242.
[59] Y.G. Habba, M. Capochichi-Gnambodoe, L. Serairi, Y. Leprince-Wang, Enhanced photocatalytic activity of ZnO nanostructure for water purification, Phys. Status Solidi Basic Res. 253 (2016) 1480–1484, https://doi.org/10.1002/pssb.201600031.
[60] J. Luan, Z. Hu, Synthesis, property characterization, and photocatalytic activity of novel visible light-responsive photocatalyst Fe2BiSbO7, Int. J. Photoenergy 2012 (2012), https://doi.org/10.1155/2012/301954.
[61] E. Parvizi, R. Tayebee, E. Koushki, M.F. Abdizadeh, B. Maleki, P. Audebert, L. Galmiche, Photocatalytic efficacy of supported tetrazine on MgZnO nanoparticles for the heterogeneous photodegradation of methylene blue and ciprofloxacin, RSC Adv. 9 (2019) 23818–23831, https://doi.org/10.1039/c9ra04702f.
[62] K.A. Isai, V.S. Shrivastava, Photocatalytic degradation of methylene blue using ZnO and 2%Fe–ZnO semiconductor nanomaterials synthesized by sol–gel method: a comparative study, SN Appl. Sci. 1 (2019) 1–11, https://doi.org/10.1007/s42452-019-1279-5.
[63] N.S. Jyothi, K. Ravichandran, Optimum pH for effective dye degradation: Mo, Mn, Co and Cu doped ZnO photocatalysts in thin film form, Ceram. Int. 46 (2020) 23289–23292, https://doi.org/10.1016/j.ceramint.2020.06.076.